Elastic Metagratings with Simultaneous Highly Efficient Control over Longitudinal and Transverse Waves for Multiple Functionalities

Jun Mei,[1] Lijuan Fan,[1] and Xiaobin Hong[2,*]

[1] *School of Physics, South China University of Technology, Guangzhou 516040, China*
[2] *School of Mechanical & Automotive Engineering, South China University of Technology, Guangzhou 510641, China*

(Received 23 January 2022; revised 19 April 2022; accepted 12 May 2022; published 1 July 2022)

Elastic metagratings that can efficiently manipulate the propagation of bulk longitudinal and transverse waves are highly desired in various applications, such as geological exploration and nondestructive detection. Here, a class of elastic metagratings consisting of a one-dimensional array of elliptical hollow cylinders carved in a steel background is proposed and studied. With the help of elastic-wave-diffraction analysis and a genetic-algorithm-based optimization approach, these intelligently designed metagratings can reflect longitudinal and transverse waves in a highly efficient and spatially separated way. Various wave-front-manipulation functionalities, such as specular reflection for longitudinal waves and anomalous reflection for transverse waves, can be simultaneously achieved with an almost perfect efficiency. Interestingly, different functionalities over both longitudinal and transverse waves can be realized by using the same cylinders with different rotation angles. Due to the nonresonant characteristics, the exhibited functionality shows robustness over both working frequencies and unit-cell configurations, which are beneficial for practical applications.

DOI: 10.1103/PhysRevApplied.18.014002

I. INTRODUCTION

A metasurface is a subwavelength-thick artificial material that can effectively control the propagation of electromagnetic waves through an intentional engineering of the phase gradient along the surface [1]; thus, it can be viewed as a two-dimensional (2D) version of a metamaterial. This notation was extended to acoustic and elastic waves [2], and various wave-front manipulation effects were demonstrated, including anomalous reflections and transmissions [3–7], retroreflections [8], cloaking, insulating, absorbing, focusing, and nonlinear effects [9–15]. Generally, metasurfaces are designed according to the generalized Snell's law [1,16], and their efficiency of wave manipulation at large diffraction angles is drastically reduced due to the impedance mismatch between the incident and scattered beams [5,6]. To this end, the concept of a metagrating was recently proposed and studied [17,18]; this is based on the diffraction-grating theory instead of the generalized Snell's law. By properly designing the scatterers in the metagratings, different diffraction orders of the scattered waves can be manipulated separately and efficiently in a controllable way. For example, the scattered-wave energy can be driven only in the desired direction with nearly unitary efficiency, even for very steep diffraction angles. It is also not necessary to discretize a fast-varying impedance or phase profile into complex implementations of meta-atoms, which is usually required in the design of metasurfaces.

Although metagratings are proposed for electromagnetic waves, they can also be applied to acoustic waves, where various wave manipulation functionalities are demonstrated, such as anomalous reflection or refraction [19–25], nonreciprocal transmission [26], multifunctional manipulation [27], and the cloaking effect [28]. In comparison, the reported progress in the field of elastic metagratings is much less. One example is the elastic metagrating proposed by Kim *et al.*, which is composed of slender and straight beams to achieve anomalous reflections of longitudinal waves in elastic plates [29]. Although many interesting studies [30–44] were reported for the control of Lamb waves or shear-horizontal (SH) waves in elastic plates, in many application scenarios, such as geological exploration and nondestructive detection, the full control of *bulk* elastic waves, including both compressional and shear-wave components, are necessary and needed. For the manipulation of bulk waves in elastic media, it is

*mexbhong@scut.edu.cn

worth mentioning that a few pioneering works were based on metasurfaces. For example, the topology optimization method is proposed to achieve anomalous reflection [45] or anomalous refraction of longitudinal elastic waves [46]. In addition, elastic metasurfaces composed of platelike waveguides connected at both ends to half-space solids are proposed to split the p wave and shear-vertical (SV) wave [47], or to achieve abnormal refraction and wave-front shape conversion of the SV wave [48]. But the simultaneous control and high-efficiency manipulation of both bulk longitudinal and transverse waves along desired directions is greatly needed and yet to be realized. It is well known that longitudinal and transverse waves will couple with and even convert into each other when they encounter scatterers, which makes the elastic-wave-scattering process more complex. Thus, the design of an elastic metagrating or metasurface is naturally more challenging, compared with the situation for scalar waves. Furthermore, for practical applications, it is often desired to manipulate the longitudinal and transverse waves in a spatially separated and highly controllable way without any unwanted crosstalk between them. It is also highly desired that various wave-front-manipulation functionalities can be achieved with an almost unitary efficiency, even for steep diffraction angles, to approach a maximized efficiency in signal processing or energy harvesting. It would be even better if the above requirements could be simultaneously satisfied by one metagrating platform with as simple a unit-cell configuration as possible.

Here, we propose a simply structured elastic metagrating that is composed of periodically arranged elliptical hollow cylinders in a steel background, as shown schematically in Fig. 1(a). With the concurrent use of elastic-wave-diffraction analysis and intelligent-optimization algorithms, we show that the simultaneous manipulation of both longitudinal and transverse waves can be realized with a very high efficiency. For example, for a normally incident longitudinal wave, only −1st-order longitudinal reflected wave and +1st-order transverse reflected wave (denoted as p_{-1} and s_1 channels, respectively) are excited with an almost perfect reflection efficiency. In addition, we find that, by simply rotating one or two cylinders in each unit cell, multifunctional wave-front-manipulation effects can be achieved, including the specular reflection of one type of wave and anomalous reflection of the other type, with a simultaneous beam-splitting effect without any crosstalk between them. Various wave-front-conversion effects are unambiguously demonstrated through full-wave numerical simulations. More interestingly, the exhibited functionality is not only valid at a single frequency or for a fixed unit-cell configuration, but also maintained over a range of working frequency and rotation angles, showing robustness that is desired for practical applications. Considering its flexible functionalities and simple structure, the proposed elastic metagrating may find potential applications in different fields, either as a planar device or as an integral component for elastic wave manipulation.

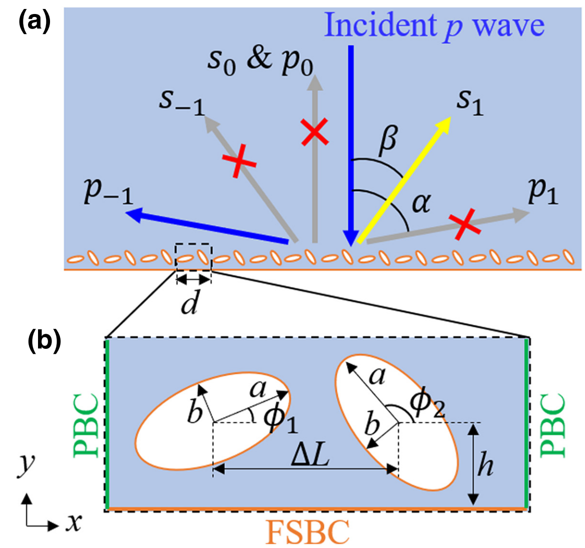

FIG. 1. Schematic diagram of the elastic wave metagrating. (a) Anomalous-reflection functionality is achieved when a longitudinal wave is normally incident onto the metagrating, so that the transverse wave is reflected only along the s_1 channel, while the longitudinal wave is reflected only along the p_{-1} channel. (b) Each unit cell consists of two elliptical hollow cylinders, with a center-to-center distance, ΔL, between them. Two cylinders have the same size and same distance, h, to the bottom surface, but have different rotation angles, ϕ_1 and ϕ_2, respectively. Free-surface boundary conditions (FSBCs) are applied for each cylinder's surface and the bottom surface of the unit cell and periodic boundary conditions (PBCs) on the left and right sides of the unit cell.

II. THEORETICAL ANALYSIS

The elastic metagrating is constructed from a one-dimensional (1D) array of elliptical hollow cylinders carved in a steel background, as shown schematically in Fig. 1(a). Each unit cell is composed of two elliptical cylinders with the same size (i.e., the same semimajor axis a and semiminor axis b) and having the same distance, h, to the bottom surface of the unit cell. Without loss of generality, free-surface boundary conditions (FSBCs) are applied for each cylinder's surface and the bottom surface of the unit cell, while PBCs are applied on the left and right sides of the unit cell. The center-to-center distance between the two cylinders is ΔL, and their rotation angles, defined as the angle between their semimajor axis a and the x axis, are ϕ_1 and ϕ_2, respectively.

According to the theory of grating diffraction, a plane wave incident onto the metagrating will be reflected into several plane-wave beams of different diffraction orders. For a longitudinal plane wave with incident angle θ_{in}, the mth-order reflected longitudinal wave (p wave) and the

nth-order reflected transverse wave (s wave) are given by

$$k_p \sin\theta_{\rm in} + m\frac{2\pi}{d} = k_p \sin\theta_{p,{\rm re}} \quad \text{(for the } m\text{th - order reflected } p \text{ wave)}, \tag{1}$$

$$k_p \sin\theta_{\rm in} + n\frac{2\pi}{d} = k_s \sin\theta_{s,{\rm re}} \quad \text{(for the } n\text{th - order reflected } s \text{ wave)}, \tag{2}$$

where $m(n)$ is the reflection order; d represents the periodicity or lattice constant; and $\theta_{p,{\rm re}}(\theta_{s,{\rm re}})$ and $k_p(k_s)$ are the reflection angle and wave number of the p (s) wave, respectively. For a normally incident ($\theta_{\rm in}=0^\circ$) longitudinal wave, for example, suppose we need to perfectly reflect the longitudinal and transverse waves, in a spatially separated way, along specific directions. To accomplish this nontrivial wave-manipulation task, we should first eliminate all possible high-order parasitic reflections. According to Eqs. (1) and (2), when the first-order reflection angles $\theta_{p_1,{\rm re}}=\alpha$ and $\theta_{s_1,{\rm re}}=\beta$ are greater than 30°, only three diffraction orders ($m=0$, ±1, and $n=0$, ±1) are available as propagating modes for either p or s waves. Then, we utilize the intelligent-optimization algorithm to *simultaneously* suppress the p_0, p_1, s_0, and s_{-1} diffraction orders to achieve the desired high-efficiency reflection along the p_{-1} and s_1 directions only. In the following, we demonstrate the design and realization of elastic metagratings for simultaneous control over six ($m, n=0,\pm1$) reflection channels. But we want to mention that the same design principle can be applied to more general situations where more diffraction orders (i.e., 9 or 12) need to be controlled and manipulated, with the price of more complicated unit-cell structures being involved. We also note in passing that the background material of the metagrating is not limited to steel. In fact, it could be aluminum, copper, or any other solid material. Here, the steel matrix is taken as an example to demonstrate the design paradigm.

In this work, we study the propagation behavior of elastic waves in a bulk material with an infinite thickness in the z direction, with the wavevector $\mathbf{k}$ confined in the x-y plane. Since the hollow cylinders are also infinitely long in the z direction, the elastic wave equation has two sets of solutions that are decoupled from each other. One set of solutions is for the shear-wave mode, the displacement of which is always parallel to the z direction, satisfying a 2D scalar wave equation, and mathematically equivalent to the solution of the acoustic wave equation. The other set of solutions has a displacement vector, $\mathbf{U}$, lying in the x-y plane, where longitudinal- and transverse-wave components can couple with and convert into each other. Thus, the latter solution is what we are interested in and focus on in this work. Let us begin with the displacement vector for a normally incident p wave, i.e., $\mathbf{U}_{p,{\rm in}}=(0,\ U_{p,y})=(0,\ u_0e^{-ik_py})$, where u_0 is the displacement's amplitude. Accordingly, the displacements for bulk longitudinal and transverse reflected waves, such as p_0, s_0, $p_{\pm1}$, and $s_{\pm1}$ channels, can be expressed as

$$\begin{aligned}
\mathbf{U}_{p_0,{\rm re}} &= (0,\ U_{p_0,y}) = (0,\ u_{p_0}e^{ik_py}),\\
\mathbf{U}_{s_0,{\rm re}} &= (U_{s_0,x},0) = (u_{s_0}e^{ik_sy},0),\\
\mathbf{U}_{p_{\pm1},{\rm re}} &= (U_{p_{\pm1},x},\ U_{p_{\pm1},y}) = (\pm\sin\alpha,\cos\alpha)u_{p_{\pm1}}\\
&\quad\times e^{i\left(\pm(2\pi/d)x+\sqrt{{k_p}^2-(2\pi/d)^2}y\right)},\\
\mathbf{U}_{s_{\pm1},{\rm re}} &= (U_{s_{\pm1},x},U_{s_{\pm1},y}) = (\mp\cos\beta,\pm\sin\beta)u_{s_{\pm1}}\\
&\quad\times e^{i\left(\pm(2\pi/d)x+\sqrt{{k_s}^2-(2\pi/d)^2}y\right)},
\end{aligned} \tag{3}$$

where u_{p_0}, $u_{p_{\pm1}}$, u_{s_0}, and $u_{s_{\pm1}}$ are the magnitudes of the corresponding displacement vectors, respectively. We define $R_{p_j}=(|u_{p_j}|^2\cos\theta_{p,{\rm re}})/\left[\sum_m(|u_{p_m}|^2\cos\theta_{p,{\rm re}})+\sum_n(|u_{s_n}|^2\cos\theta_{s,{\rm re}})\right]$ and $R_{s_j}=(|u_{s_j}|^2\cos\theta_{s,{\rm re}})/\left[\sum_m(|u_{p_m}|^2\cos\theta_{p,{\rm re}})+\sum_n(|u_{s_n}|^2\cos\theta_{s,{\rm re}})\right]$, respectively, as the reflection efficiency of the jth-order ($j=0,\ \pm1$) p and s waves with respect to the total wave flux. For easy discussion, we also define the function $EP_j=(|u_{p_j}|^2\cos\theta_{p,{\rm re}})/\sum_m(|u_{p_m}|^2\cos\theta_{p,{\rm re}})$ as the normalized reflectivity of the jth-order p wave with respect to the p-wave flux, and similarly $ES_j=(|u_{s_j}|^2\cos\theta_{s,{\rm re}})/\sum_n(|u_{s_n}|^2\cos\theta_{s,{\rm re}})$ as the normalized reflectivity of the jth-order s wave with respect to the s-wave flux. In this work, we use the commercial software package COMSOL Multiphysics for full-wave numerical simulations and reflectivity calculations, which are based on the finite-element method.

We utilize an intelligent-optimization method based on the genetic algorithms (GAs) to suppress unwanted diffraction orders, such as p_0, p_1, s_0, and s_{-1}. The GA is an evolutionary algorithm designed to search for optimal solutions through simulating the evolutionary process in nature by relying on biologically inspired operators, such as mutation, crossover, and selection [22,26,27]. By evaluating the fitness of every individual in the population of each generation, the more fit individuals are stochastically selected and are then used in the next iteration. The algorithm usually terminates when either a maximum number of generations has been produced or a satisfactory fitness level has been reached. When applying the GA, appropriate optimization objectives (defined as the fitness functions) are formulated according to specific requirements, and by optimizing the structural parameters (denoted as the optimization variables), researchers can finally obtain a set of parameters for the desired solution (such as the wave-front-manipulation effect). In this article, we take the geometric parameters (a, b, h, ΔL, ϕ_1, and ϕ_2) of the two elliptical cylinders as the optimization variables and set the normalized reflectivity, EP_{-1} and ES_1, as the optimization targets. To ensure that the reflected-wave energy does not concentrate in the

p wave only or in the s wave only, we set the preconditions $R_{p_{-1}} > 20\%$ and $R_{s_1} > 20\%$. In this way, the optimization targets EP_{-1} and ES_1 can converge to 100% simultaneously. With the help of the GA, we can quickly find the optimized structural parameters that satisfy the desired wave-front-manipulation functionalities, as demonstrated in the following discussions.

III. RESULTS

To be more specific, we assume that the frequency of the incident p wave is $f = 80$ kHz. The background material is steel, with its mass density, Young's modulus, and Poisson ratio being $\rho = 7874\ \mathrm{kg/m^3}$, $E = 211$ GPa, and $\nu = 0.29$, respectively. The corresponding longitudinal- and transverse-wave velocities are $c_p = \sqrt{((1-\nu)E)/((1+\nu)(1-2\nu)\rho)} = 5926$ m/s and $c_s = \sqrt{E/(2(1+\nu)\rho)} = 3223$ m/s, respectively. According to Eqs. (1) and (2), for a normally incident ($\theta_{\mathrm{in}} = 0$) plane p wave, the directions of the first-order ($m = 1$) reflected p wave and first-order ($n = 1$) reflected s wave can be calculated from

$$\frac{2\pi}{d} = k_p \sin\theta_{p,\mathrm{re}} = \frac{2\pi}{\lambda_p} \sin\theta_{p,\mathrm{re}}, \tag{4}$$

$$\frac{2\pi}{d} = k_s \sin\theta_{s,\mathrm{re}} = \frac{2\pi}{\lambda_s} \sin\theta_{s,\mathrm{re}}, \tag{5}$$

where λ_p and λ_s are the wavelengths of the p wave and s wave in steel at the working frequency, respectively. Without loss of generality, let us assume that the desired reflection angle for the p wave is $\theta_{p,\mathrm{re}} = \alpha = 70^\circ$. From Eqs. (4) and (5), the reflection angle for the s wave can be determined as $\theta_{s,\mathrm{re}} = \beta = \sin^{-1}((\lambda_s/\lambda_p)\sin\theta_{p,\mathrm{re}}) = 30.7^\circ$. For both p and s waves, the period, d, of the unit cell must be the same, which is $d = \lambda_p/\sin\theta_{p,\mathrm{re}} = \lambda_s/\sin\theta_{s,\mathrm{re}} = 78.83$ mm. As stated previously, among all six reflection channels, we need to intentionally suppress the $m = 0$, 1 and $n = 0, -1$ diffraction orders to achieve the anomalous-reflection functionality: the reflected wave goes out along the p_{-1} and s_1 channels only. To achieve this goal, we need to utilize the design degrees of freedom (DOFs) rendered by the six geometrical parameters, which are the semimajor axis a, semiminor axis b, rotation angles ϕ_1 and ϕ_2, vertical distance h, and horizontal distance ΔL of the two cylinders.

In applying the GA, we set the optimization objective as $L = (|1 - EP_{-1}| + |1 - ES_1|) \times 100$, which is also the fitness function for each individual. In each generation, the minimum value of L is called the best fitness function of that generation. Accordingly, the detailed hyperparameters are as follows: (1) the size of the population is 100; (2) the crossover fraction is 0.9; (3) the migration fraction is 0.3; (4) the migration interval is 5; and (5) the algorithm stops if the relative change in the best fitness function, L_{best}, over 50 generations is less than or equal to 1.0×10^{-6}. The maximum number of iterations before the algorithm halts is 1000.

In this case, we observe that L_{best} drops below 10.69 from the 93rd generation, and the GA terminates at the 143rd generation, where the relative change of L_{best} over 50 generations is less than 1.0×10^{-6}, satisfying the preset stop condition. After applying the optimization algorithm, we can achieve very high reflection efficiencies for both p_{-1} and s_1 channels, i.e., $R_{p_{-1}} = 45.6\%$ and $R_{s_1} = 51.9\%$ (with $EP_{-1} = 98.4\%$ and $ES_1 = 96.6\%$, respectively). Such high efficiency is achieved because the design DOFs (six) are enough for the simultaneous control of six diffraction orders. As a general design principle, one must ensure that the design DOFs of the unit cell (i.e., the size, orientation, and position of the elliptical cylinders) are equal to or larger than the number of diffraction-channel efficiencies to be controlled [49]. In this example, the optimized parameters are $a = 9.95$ mm, $b = 3.37$ mm, $h = 10.95$ mm, $\Delta L = 35.30$ mm, $\phi_1 = 9.9^\circ$, and $\phi_2 = 135.8^\circ$, which means that the thickness of the metagrating is only $0.27\lambda_p$ or $0.50\lambda_s$ at the working frequency.

In the finite-element-based numerical simulations, the diffraction efficiency is calculated with a mesh size of $\lambda_p/50$. In fact, we calculate the diffraction efficiency with different sizes of mesh (such as $\lambda_p/35$, $\lambda_p/50$, and $\lambda_p/100$) and observe that the mesh size of $\lambda_p/50$ is fine enough to guarantee a converged result. The amplitude of the displacement vector is plotted in Fig. 2(c), where white and yellow arrows denote p and s waves, respectively. Obviously, the desired anomalous-reflection functionality is achieved with an almost perfect efficiency. Thus, we see that the proposed elastic metagrating indeed has the capability of reflecting and separating the longitudinal and transverse waves simultaneously along their desired directions in a highly efficient way. Since different diffraction channels can carry different wave signals, this anomalous-reflection functionality has unique advantages for elastic-wave-signal multiplexing and demultiplexing when the DOFs rendered by the coexistence of p and s waves are fully utilized.

To gain further insights into the properties of the elastic metagrating, we study the influence of the two cylinders' rotation angle, $\delta\phi$, on the reflection efficiencies along various channels. We start from the set of optimized parameters used in Fig. 2(c), i.e., $\phi_1 = 9.9^\circ$ and $\phi_2 = 135.8^\circ$, which is defined as the initial configuration with $\delta\phi = 0^\circ$. Then we rotate the two elliptical cylinders *simultaneously* by the same angle, $\delta\phi$, so that after rotation the two cylinders arrive at new configurations of $\phi_1 = 9.9^\circ + \delta\phi$ and $\phi_2 = 135.8^\circ + \delta\phi$, respectively. In the process of rotating, all other geometrical parameters (a, b, h, and ΔL) remain unchanged, as shown schematically in Fig. 2(a). The reflection-efficiency curves

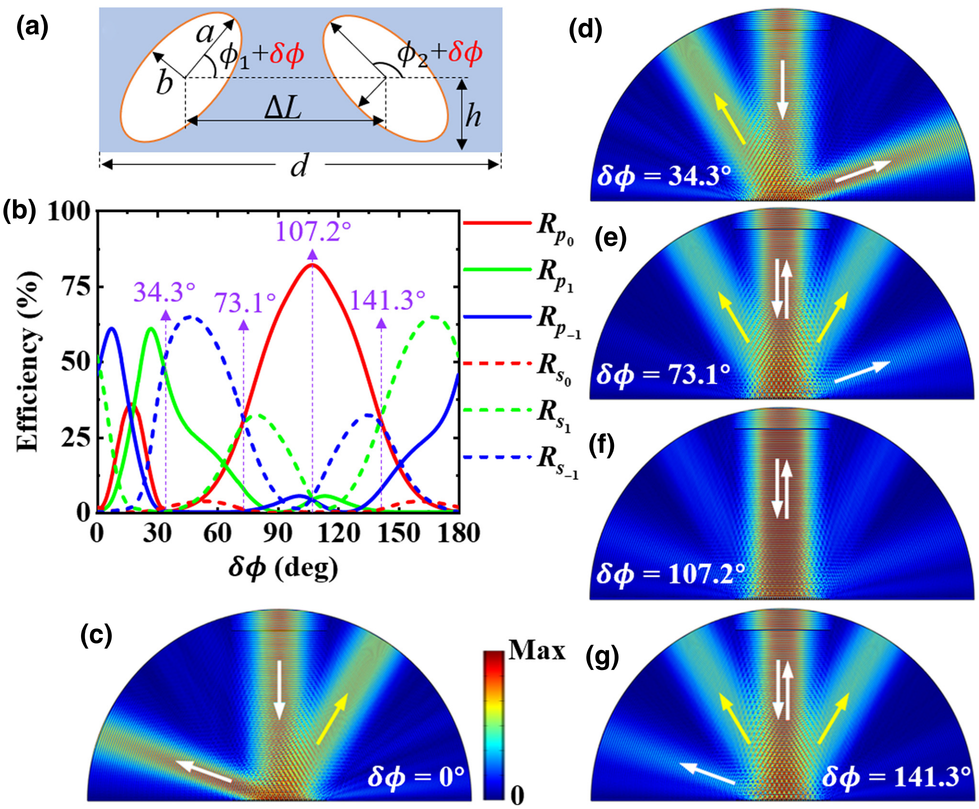

FIG. 2. Influence of the common rotation angle, $\delta\phi$, on reflectance. (a) Schematic diagram shows the simultaneous rotation of two elliptical cylinders. (b) Reflection efficiency for six diffraction orders (R_{p_0}, R_{p_1}, $R_{p_{-1}}$, R_{s_0}, R_{s_1}, and $R_{s_{-1}}$) as a function of $\delta\phi$. Amplitude of the displacement vector when a p wave is normally incident onto the grating for different unit-cell configurations: (c) $\delta\phi = 0°$, (d) $\delta\phi = 34.3°$, (e) $\delta\phi = 73.1°$, (f) $\delta\phi = 107.2°$, and (g) $\delta\phi = 141.3°$. White and yellow arrows indicate the propagation directions of p wave and s wave, respectively.

for various diffraction orders are plotted in Fig. 2(b) as a function of $\delta\phi$. For $\delta\phi = 0°$, the two cylinders stay at their initial optimized positions, with $R_{p_{-1}}$ (blue solid line) and R_{s_1} (green dashed line) being two dominating reflection orders. With the increase of $\delta\phi$, R_{p_0} (red solid line) and R_{p_1} (green solid line) begin to increase rapidly. It is worth noting that, when $\delta\phi = 17.0°$, there are only reflected p waves left, with $R_{p_0} = 35.9\%$, $R_{p_1} = 29.8\%$, and $R_{p_{-1}} = 31.0\%$, while all s waves are highly suppressed in the reflection.

With a further increase of $\delta\phi$, R_{p_0} and $R_{p_{-1}}$ decay rapidly, while R_{p_1} (green solid line) and $R_{s_{-1}}$ (blue dashed line) increase rapidly and become gradually dominant. In particular, we have $R_{p_1} + R_{s_{-1}} > 95\%$ when $\delta\phi \in [30.9°, 41.0°]$. Take $\delta\phi = 34.3°$ as an example, as marked by the vertical purple arrow in Fig. 2(b), we have $R_{p_1} = 45.6\%$ and $R_{s_{-1}} = 51.8\%$, with the corresponding displacement amplitude plotted in Fig. 2(d). Compared with the case of $\delta\phi = 0°$, we find that, after rotation, the p wave is switched from the p_{-1} channel to the p_1 channel, and the s wave is switched from s_1 to s_{-1} simultaneously.

As $\delta\phi$ further increases, it is interesting to note that the efficiency curves for all six channels have a symmetrical pattern with respect to the vertical line of $\delta\phi = 107.2°$. At $\delta\phi = 107.2°$, $R_{p_{-1}}$ is identical to R_{p_1} and $R_{s_{-1}}$ is the same as R_{s_1}, but none of them contribute substantially to the total energy flux. Instead, most of the reflected waves are driven into the p_0 channel (i.e., the retroreflection functionality) with a very high efficiency, $R_{p_0} = 82.0\%$, with corresponding displacement amplitude shown in Fig. 2(f). Furthermore, the cases of $\delta\phi = 73.1°$ and $141.3°$ are also interesting. First, we note that $107.2°$ is in the middle between $73.1°$ and $141.3°$. We find from Fig. 2(b) that R_{p_0}, R_{s_1}, and $R_{s_{-1}}$ are three dominant channels for both $\delta\phi = 73.1°$ and $141.3°$, and the reflection efficiency along these three channels has nearly the same value (i.e., the energy is almost equally distributed). Thus, the reflected beams for $\delta\phi = 73.1°$ and $141.3°$ must be symmetrical with respect to each other about the normal of the metagrating. Full-wave numerical simulations support our expectation, as clearly shown in Figs. 2(e) and 2(g), where the beam-splitting functionality for the s wave and specular reflection effect for the p wave is simultaneously achieved. Thus, different wave-manipulation functionalities can be switched by rotating the elliptical cylinders with a large rotation angle, $\delta\phi$.

From the above discussions, we see that, when we simultaneously rotate the two elliptical cylinders by the same angle, $\delta\phi$, various wave-front-manipulation functionalities can be generated. In the following, we show that a similar effect can be obtained when we rotate only one cylinder but keep the other unchanged. Let us begin again with the initial (and also optimized) configuration that is demonstrated in Fig. 2(c). Then we rotate one cylinder by varying ϕ_1 and keep the other unchanged with $\phi_2 \equiv 135.8^\circ$, as shown schematically in Fig. 3(a). In this process, all other structural parameters remain fixed with $a = 9.95$ mm, $b = 3.37$ mm, $h = 10.95$ mm, and $\Delta L = 35.30$ mm. Figure 3(b) shows the reflection efficiency as a function of ϕ_1, where $\phi_1 = 9.9^\circ$ corresponds to the initial configuration in Fig. 2(c). We observe that a high-efficiency abnormal-reflection phenomenon ($R_{p_{-1}} + R_{s_1} > 95\%$) can be achieved within the angle range of $\phi_1 \in [-12.6^\circ, 22.6^\circ]$, which means that the metagrating's functionality is robust against a small rotation angle. Taking $\phi_1 = 0^\circ$ as an example, the reflected waves go back almost exclusively along p_{-1} and s_1 channels with $R_{p_{-1}} = 43.0\%$ and $R_{s_1} = 54.0\%$. The corresponding displacement amplitude is plotted in Fig. 3(c), where a high-efficiency abnormal reflection of both p and s waves along different directions is realized. Another example is $\phi_1 = 60^\circ$, which is marked by the purple arrow in Fig. 3(b). For this case, the reflected longitudinal wave is dominated by the p_0 channel with $R_{p_0} = 39.4\%$, and the reflected transverse wave is mainly along the s_{-1} channel with $R_{s_{-1}} = 42.9\%$. The corresponding numerical simulation results of displacement amplitudes are shown in Fig. 3(d), where the high-efficiency reflection along the p_0 and s_{-1} channels is observed. As ϕ_1 continues to increase, more and more energy is driven into the p_0 channel. At $\phi_1 = 117.8^\circ$, R_{p_0} reaches its maximum value of 82.5%, which implies a strong retroreflection effect.

Next, we show the effect on reflectance when ϕ_1 is fixed at 9.9° but ϕ_2 is varied, where the initial configuration of $\phi_2 = 135.8^\circ$ is discussed in Fig. 2(c). Through analysis, we find that a high-efficiency anomalous

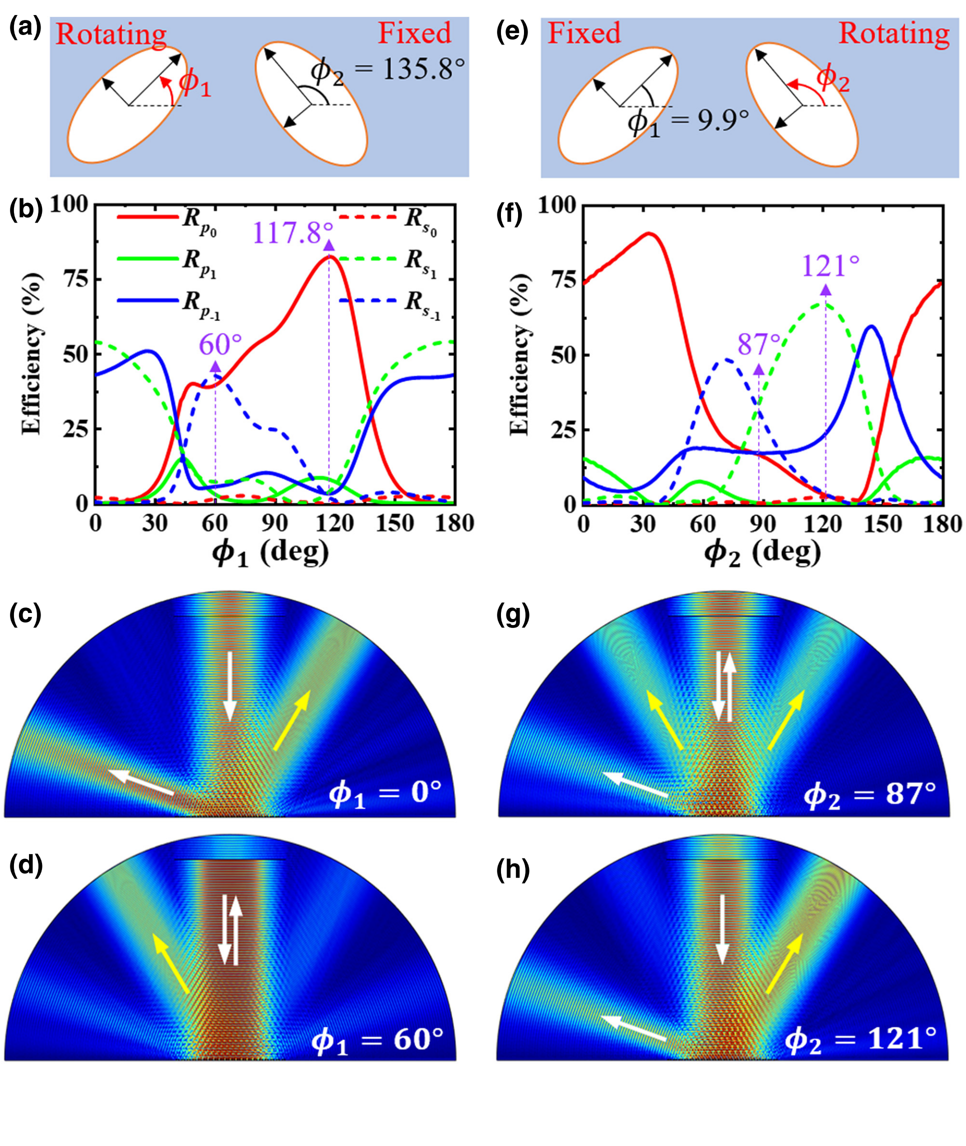

FIG. 3. Influence of one cylinder's rotation angle on reflectance. (a) Schematic diagram shows the situation where ϕ_1 is varied while ϕ_2 is fixed at 135.8°, with the corresponding reflection efficiency plotted in (b). (c),(d) Displacement amplitudes for $\phi_1 = 0^\circ$ and $\phi_1 = 60^\circ$, respectively. (e),(f) Similar to (a),(b), except that now ϕ_2 is varied while ϕ_1 is fixed at 9.9°. (g),(h) Displacement amplitudes for $\phi_2 = 87^\circ$ and $\phi_2 = 121^\circ$, respectively.

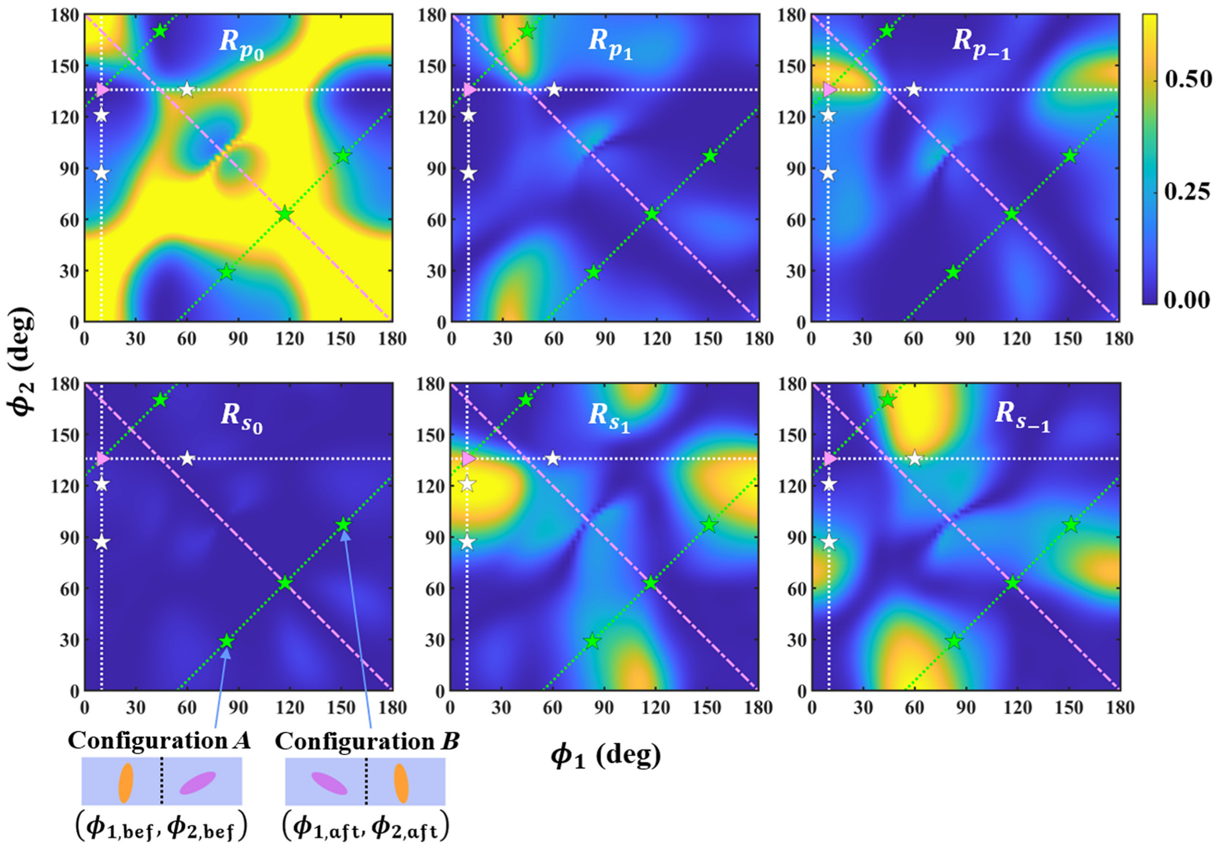

FIG. 4. Reflection efficiency for various diffraction orders (R_{p_0}, R_{p_1}, $R_{p_{-1}}$, R_{s_0}, R_{s_1}, and $R_{s_{-1}}$) as a function of rotation angles ϕ_1 and ϕ_2 of the two cylinders. Pink triangle represents the optimized solution of $(\phi_1, \phi_2) = (9.9°, 135.8°)$, as demonstrated in Fig. 2(c). Green dotted lines and green stars correspond to the cases shown in Figs. 2(d)–2(g). In particular, two unit-cell configurations corresponding to two green stars [i.e., (83°, 28.9°) and (151.2°, 97.1°)] are shown in the inset to exhibit the spatial symmetry between them. White dotted lines and white stars correspond to the cases shown in Fig. 3.

reflection ($R_{p_{-1}} + R_{s_1} > 90\%$) can be maintained within the angle range of $\phi_2 \in [120.8°, 142.5°]$. There are also interesting cases outside this angle range. We pick two angles as examples, as shown by the purple arrows in Fig. 3(f). When $\phi_2 = 87.0°$, p_1 and s_0 are completely suppressed, while s_1 and s_{-1} contribute substantially to the total energy flux, with $R_{s_1} = 31.7\%$, $R_{s_{-1}} = 32.8\%$, $R_{p_0} = 17.0\%$, and $R_{p_{-1}} = 17.3\%$. Full-wave numerical simulation results in Fig. 3(g) clearly show the specular- and anomalous-reflection functionality for the p wave, as well as the beam-splitting effect for the s wave. Another example is $\phi_2 = 121.0°$, where s_1 is the most important diffraction order and $R_{s_1} + R_{p_{-1}} > 90\%$, with all other diffraction channels strongly suppressed. The corresponding displacement amplitude is shown in Fig. 3(h). Thus, all the cases demonstrated in Figs. 2 and 3 show that the functionalities of the elastic metagrating can be controlled by simply rotating one or two cylinders in each unit cell, which is beneficial for some application scenarios, where multiple distinct functionalities are required for a single-grating platform. In this regard, potential applications for the elastic metagrating are discussed in Appendix C.

To gain a thorough and complete understanding of the metagrating, we calculate the reflection efficiencies R_{p_0}, R_{p_1}, $R_{p_{-1}}$, R_{s_0}, R_{s_1}, and $R_{s_{-1}}$ for all possible rotation angles, and plot the results as 2D graphs in Fig. 4, with the x axis and y axis representing ϕ_1 and ϕ_2, respectively. We observe that R_{s_0} is always strongly suppressed, while R_{p_0} is only strongly suppressed in some regions. Actually, when a p wave is normally incident on the metagrating, it is natural to expect that, in most scenarios, the wave energy is reflected back along the p_0 channel, simply because this is the direction of specular reflection. This is the reason why R_{p_0} usually takes a large value and is suppressed only in some regions. It is also noted that, for both incident and reflected p waves along the y direction, the corresponding displacement vector is parallel to the y direction, due to the longitudinal-wave character of the p wave. In contrast, for a reflected s wave along the s_0 channel, its displacement vector is perpendicular to the y direction, due to its transverse-wave character. Thus, the displacement

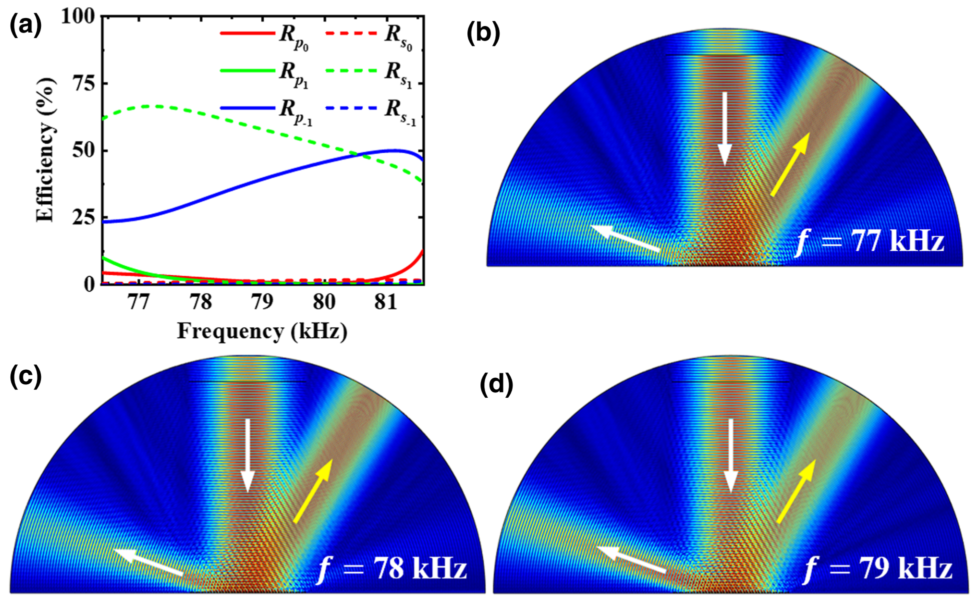

FIG. 5. Bandwidth of the elastic metagrating. (a) Reflection-efficiency spectrum, where $f = 80$ kHz is the initially optimized working frequency. Displacement amplitude when a longitudinal wave is incident onto the grating with different frequencies: (b) $f = 77$ kHz, (c) $f = 78$ kHz, and (d) $f = 79$ kHz.

vectors for the normally incident p wave and reflected s_0 wave are orthogonal to each other. Therefore, it is difficult for a normally incident p wave to excite a reflected s_0 wave. This is the reason why R_{s_0} is always strongly suppressed.

Consistently, $R_{p_{\pm 1}}$ and $R_{s_{\pm 1}}$ appear only in the regions where R_{p_0} is suppressed. R_{p_1} and $R_{s_{-1}}$ have overlapping high-value regions, just like $R_{p_{-1}}$ and R_{s_1} do. Interestingly, we find that both patterns of R_{p_0} and R_{s_0} are symmetrical with respect to the pink dashed-dotted line, the equation of which can be written as $(\phi_1 + \phi_2)/2 = l \times 90^\circ$ (l is an integer). Let us arbitrarily select any two configurations that are symmetrical about the pink line and plot their unit-cell structures schematically in the inset of Fig. 4. Obviously, configuration A can be mapped into configuration B (and vice versa) if a mirror operation is taken with respect to the (y-directional) black dashed line. But both p_0 and s_0 reflection channels are along the y direction. Therefore, configurations A and B must share the same R_{p_0} and R_{s_0}, as long as they are mirror images of each other.

In addition, the mirror image of R_{p_1} with respect the pink dashed-dotted line is exactly the same as $R_{p_{-1}}$. A similar relationship exists between R_{s_1} and $R_{s_{-1}}$. In fact, such a mirror-image rule is valid between any two points $(\phi_{1,\text{bef}}, \phi_{2,\text{bef}})$ and $(\phi_{1,\text{aft}}, \phi_{2,\text{aft}})$ on the 2D (ϕ_1, ϕ_2) plane as long as $(\phi_{1,\text{bef}} + \phi_{2,\text{aft}})/2 = (\phi_{1,\text{aft}} + \phi_{2,\text{bef}})/2 = l \times 90^\circ$. Here $(\phi_{1,\text{bef}}, \phi_{2,\text{bef}})$ and $(\phi_{1,\text{aft}}, \phi_{2,\text{aft}})$ are the angles of two elliptical cylinders before and after rotation, respectively. As mentioned previously, configurations A and B [corresponding to $(\phi_1, \phi_2) = (83^\circ, 28.9^\circ)$ and $(151.2^\circ, 97.1^\circ)$] are such examples, where the symmetrical relationship between two cylinders before and after rotation is evident, which is nothing but the abovementioned mirror-image rule.

The pink triangle in Fig. 4 represents the optimized values of ϕ_1 and ϕ_2 (i.e., $\phi_1 = 9.9^\circ$ and $\phi_2 = 135.8^\circ$), which fall in the region where bright (i.e., high value) $R_{p_{-1}}$ and bright R_{s_1} overlap. A green dotted line (from lower left to upper right) passes through the pink triangle, and the four green stars correspond to the curves in Fig. 2(b). Here, the pink triangle represents $\delta\phi = 0^\circ$, and the four green stars represent $\delta\phi = 34.3^\circ$, 73.1°, 107.2°, and 141.3°. It is easy to find from Fig. 4 that $\delta\phi = 0^\circ$ (pink triangle) and 34.3° (green star) and $\delta\phi = 73.1^\circ$ and 141.3° are pairwise symmetrical with respect to the pink dashed-dotted line. In other words, the dominant diffraction orders are switched from the p_{-1} and s_1 channels at $\delta\phi = 0^\circ$ to the p_1 and s_{-1} channels at $\delta\phi = 34.3^\circ$. But the p_0 and s_0 diffraction orders are strongly suppressed, regardless of $\delta\phi = 0^\circ$ or 34.3°. The simulation results in Figs. 2(c) and 2(d) clearly show this interchange behavior of the corresponding diffraction channels. Likewise, the green stars with $\delta\phi = 73.1^\circ$ and 141.3° have similar relationships. Another green star with $\delta\phi = 107.2^\circ$ is exactly on the pink dashed-dotted line, because here $(\phi_1 + \phi_2)/2 = (9.9^\circ + 135.8^\circ)/2 + \delta\phi = 180^\circ$, so that R_{p_0} contributes most substantially to the reflected energy flux, and all other diffraction orders are strongly suppressed.

In addition, the two white dotted lines cross each other at the pink triangle. They are perpendicular to each other and correspond to Figs. 3(b) and 3(f), respectively. To be more specific, the horizontal white dotted line represents

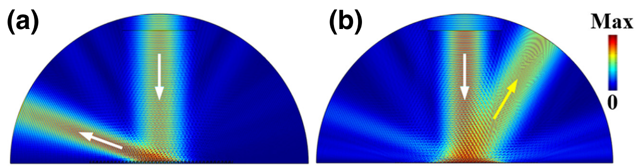

FIG. 6. Elastic metagrating with pure-mode conversion functionality. (a) Only p wave is reflected when a p wave is normally incident on the metagrating, with geometrical parameters of $a = 27.08$ mm, $b = 5.61$ mm, $h = 29.52$ mm, $\Delta L = 47.49$ mm, $\phi_1 = 86.0°$, and $\phi_2 = 64.4°$. Anomalous-reflection efficiency along the p_{-1} channel can be as high as 96.8%. (b) Only s wave is reflected when a p wave is normally incident on the metagrating, with corresponding geometrical parameters of $a = 8.21$ mm, $b = 5.97$ mm, $h = 8.31$ mm, $\Delta L = 42.46$ mm, $\phi_1 = 55.5°$, and $\phi_2 = 116.6°$. Mode-conversion efficiency from p_0 channel to s_1 channel is 92.6%.

the situation when ϕ_2 is fixed while ϕ_1 is varied. The white star on this horizontal line corresponds to $(\phi_1, \phi_2) = (60°, 135.8°)$. From Fig. 4, we notice that this white star falls in the bright regions of both R_{p_0} and $R_{s_{-1}}$, which is consistent with the efficiency curves in Fig. 3(b) and the displacement field in Fig. 3(d). The vertical white dotted line corresponds to the scenario where ϕ_1 is fixed but ϕ_2 is varied. The two white stars on the vertical line denote the cases of $(\phi_1, \phi_2) = (9.9°, 87°)$ and $(9.9°, 121°)$, respectively, as discussed in Fig. 3. Furthermore, the elastic metagrating can be utilized to realize a pure-mode conversion and the mixed-mode separation, with corresponding examples presented in Figs. 6 and 7 of Appendix A.

In the above discussions, we demonstrate the effect of rotating one or two elliptical cylinders in each unit cell. Next, we show that the abnormal-reflection effect can be maintained, even when the operating frequency is tuned. The results are shown in Fig. 5(a), where we can observe that the p_{-1} and s_1 channels are dominant in the frequency range $f \in [77, 81.4]$kHz, with corresponding $R_{p_{-1}} + R_{s_1} > 90\%$ over a bandwidth of 4.4 kHz. The corresponding displacement amplitudes are plotted in Figs. 5(b)–5(d), respectively, for frequencies $f = 77$, 78, and 79 kHz, where a satisfying wave-manipulation effect is observed. For some realistic application scenarios, the wave-manipulation functionality is desired to be maintained over a range of frequency, instead of at a fixed frequency. Although we do not intentionally optimize the working bandwidth in the first place, the elastic metagrating naturally exhibits a working bandwidth of 5.5%, due to its inherent nonresonant characteristics. We expect that the working bandwidth can be further increased if we give it a higher priority when applying the GA. Finally, in Appendix B we show that the elastic metagrating can exhibit a similar wave-manipulation functionality for a transverse incident wave.

IV. CONCLUSION

We propose a design paradigm for elastic metagratings based on elastic-wave-diffraction analysis and an intelligent-optimization algorithm. The designed elastic metagrating has a simple structure and is composed of a 1D array of elliptical hollow cylinders embedded in a steel background. With this elastic metagrating, the longitudinal- and transverse-wave modes can be manipulated with an almost unitary efficiency and in a spatially separated way without any crosstalk. By rotating the cylinders in each unit cell, distinct wave-front-manipulation functionalities can be achieved with very high efficiencies. Furthermore, these functionalities are robust with respect to both working frequencies and unit-cell configurations, making the proposed metagrating a potential candidate for various application scenarios, such as geological exploration and nondestructive structural detection.

ACKNOWLEDGMENTS

This work is supported by the Guangdong Basic and Applied Basic Research Foundation (Grant No. 2021A1515010322) and the Guangdong Province Key Research & Development Program (Grant No. 2020B0404010001).

APPENDIX A: FUNCTIONALITY OF PURE-MODE CONVERSION AND MIXED-MODE SEPARATION

Here, we show that the metagrating can be utilized to realize a pure-mode conversion or mixed-mode separation. For the mode-conversion functionality, we show two examples. In the first one, we demonstrate that the reflected field is a pure p wave (p_{-1}) with all s waves completely suppressed, when a p wave is normally incident on the metagrating. As shown in Fig. 6(a), a high-efficiency anomalous reflection along the p_{-1} channel is achieved.

In the second example, we show that the reflected field is a pure s wave (s_1) with all p waves completely suppressed, when a p wave is normally impinging on the metagrating. As shown in Fig. 6(b), a high mode-conversion efficiency from the p_0 channel to the s_1 channel is obtained.

In addition, the metagrating can be utilized to realize the separation of mixed modes, and one example is shown in Fig. 7. When a mixed elastic mode contains both longitudinal- and transverse-wave components is normally incident on the metagrating, the reflected p wave is separated from the reflected s wave in a highly efficient way such that the p wave propagates only along the p_{-1} channel and the s wave only along the s_1 channel.

APPENDIX B: METAGRATING FOR A TRANSVERSE INCIDENT WAVE

Here, we demonstrate the anomalous-reflection effect when a transverse wave is incident on the metagrating.

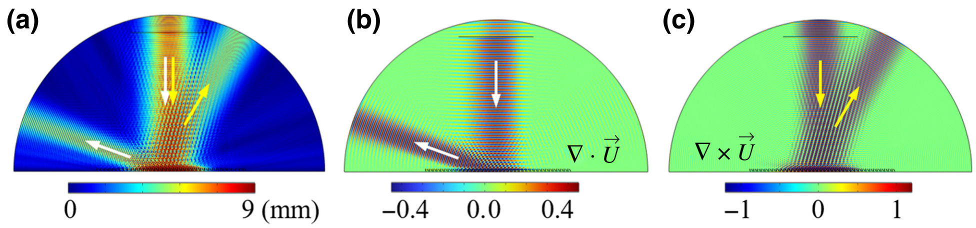

FIG. 7. Separation of mixed modes. (a) Amplitude of the displacement field. (b),(c) Divergence and curl of the displacement field, respectively, which correspond to the longitudinal- and transverse-wave fields. Geometrical parameters are $a = 27.99$ mm, $b = 2.52$ mm, $h = 39.44$ mm, $\Delta L = 44.25$ mm, $\phi_1 = 98.6°$, and $\phi_2 = 123.0°$. Anomalous-reflection efficiencies along the p_{-1} and s_1 channels are 46.7% and 50.0%, respectively.

An example is shown in Fig. 8, where the structural parameters of the unit cell are obtained by applying the GA, with $a = 11.80$ mm, $b = 4.63$ mm, $h = 71.89$ mm, $\Delta L = 24.67$ mm, $\phi_1 = 54.0°$, and $\phi_2 = 32.3°$. In addition, we also study the response of the metagrating when the two elliptical cylinders are simultaneously rotated by a common angle, $\delta\phi$. In Fig. 8(a), the reflection efficiency for each diffraction order is plotted as a function of $\delta\phi$ at $f = 80$ kHz. When $\delta\phi = 0°$ (corresponding to the initial optimized configuration), $R_{s_1} = 55.6\%$ and $R_{p_{-1}} = 42.5\%$ are the two dominating orders, and other reflection orders are highly suppressed, as verified by the displacement amplitude shown in Fig. 8(b). We also observe that R_{s_1} (green solid line) and $R_{s_{-1}}$ (blue solid line) are symmetrical with respect to $\delta\phi = 47.0°$, and there is a similar symmetrical relationship between R_{p_1} and $R_{p_{-1}}$. When $\delta\phi = 47°$, almost all of the incident-wave energy is reflected into the s_0 channel with $R_{s_0} = 94.2\%$. It is also interesting to note that this high-efficiency retroreflection ($R_{s_0} > 90\%$) effect can be maintained in the rotation-angle range of $\delta\phi \in [38.3°, 55.4°]$. When $\delta\phi = 94.0°$, $R_{s_{-1}} = 55.5\%$, and $R_{p_1} = 42.7\%$ are dominating reflection channels, while R_{s_0}, R_{s_1}, and $R_{p_{-1}}$ are strongly suppressed. Compared with the case of $\delta\phi = 0°$, the reflected transverse wave at $\delta\phi = 94°$ is switched from the s_1 channel to s_{-1}, and the reflected longitudinal wave is switched from p_{-1} to p_1.

APPENDIX C: POTENTIAL APPLICATIONS

Here, we introduce a concrete application scenario for the metagrating. In the first place, we want to note that, although our original design is based on an elastic medium that is infinite in the z direction, it is also applicable to the situation when the system has a finite thickness in the z direction. Let us consider an elastic thin plate as an example. It is well known that, in the low-frequency region, the S_0 mode (a symmetrical Lamb-wave mode with the displacement vector parallel to the wave vector, $\vec{k}$) and SH_0 mode (a shear horizontal wave mode with the displacement vector perpendicular to $\vec{k}$) have a good correspondence to bulk longitudinal and shear waves, respectively [41]. Therefore, our work can be directly transplanted to elastic systems with finite thickness, and it may find practical applications in corresponding scenarios.

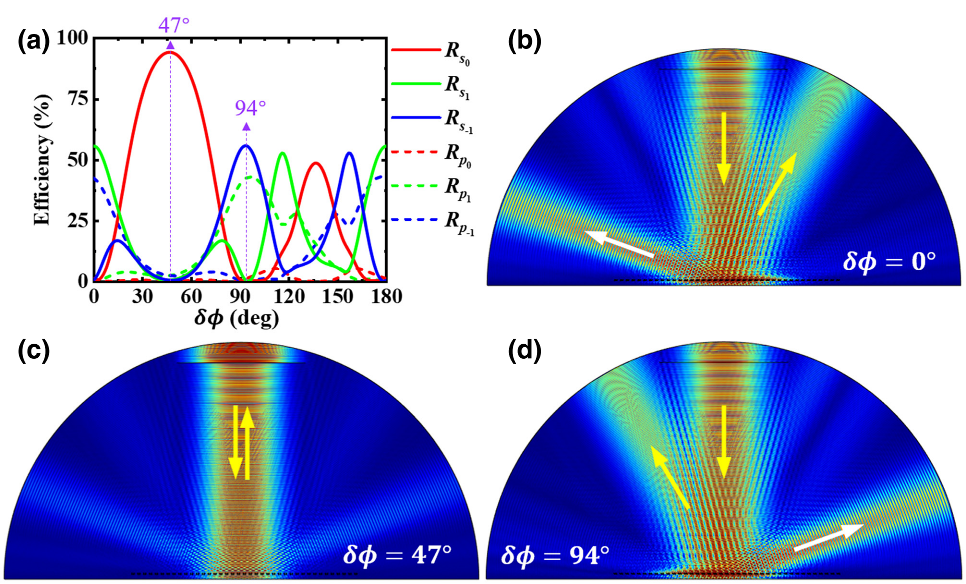

FIG. 8. Elastic metagrating for a transverse incident wave. (a) Reflection efficiency for various diffraction orders as a function of the common rotation angle, $\delta\phi$, of the two cylinders. Displacement amplitudes when a transverse wave is incident onto the grating with different unit-cell configurations: (b) $\delta\phi = 0°$, (c) $\delta\phi = 47°$, and (d) $\delta\phi = 94°$. Yellow and white arrows indicate the propagation directions of transverse and longitudinal waves, respectively.

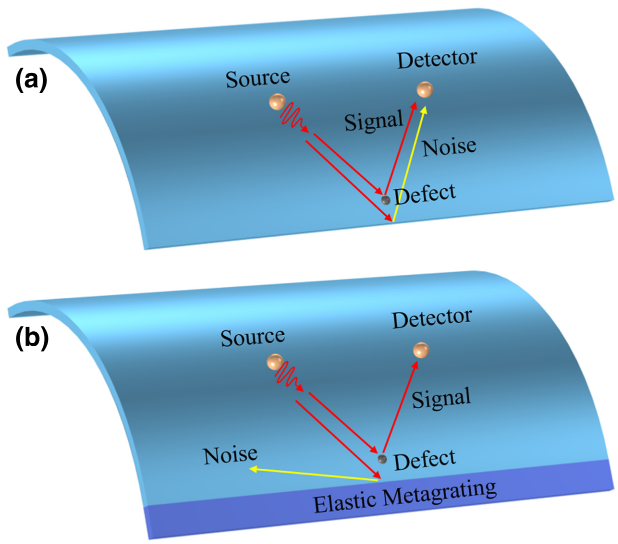

FIG. 9. Application of elastic metagrating in structural health monitoring. (a) Desired signals and background noise are mixed together. (b) Noise is spatially separated from the signals if a metagrating is introduced at the boundary of the aircraft component.

To be more specific, the metagrating's functionality of high-efficiency mode conversion between longitudinal- and transverse-wave modes is desired in fields such as structural health monitoring. In the quality inspection and analysis of a workpiece, for example, it is required to evaluate the size, shape, and location of the defects (such as pores, slag inclusions, cracks, and fatigue failures). It is common that a fatigue failure is close to the boundary of an aircraft structural component, as shown in Fig. 9(a), so that the wave signal (emitted by the source) scattered directly by the fatigue failure (defined as the desired signals, marked as red arrows) and that reflected by the component boundary (defined as noises, marked as the yellow arrow) are usually mixed together, which leads to a lower signal-to-noise ratio at the detector and makes it difficult to accurately evaluate the fatigue failure. Thus, if an elastic metagrating is introduced at the boundary of the aircraft component, we can intentionally control the wave reflected by the boundary in a desired way. For example, the reflected wave can be diffracted into a direction away from the detector, as shown by the yellow arrow in Fig. 9(b), so that noise is spatially separated from the desired signals. Or the reflected wave can be completely converted into a different wave mode (e.g., s wave) from the incident-wave signals (p wave), so that the desired signals and background noise belong to different wave modes. In either case, the detector can easily distinguish signals from noise, and it helps to greatly improve the inspection results of the workpiece.

[1] N. Yu, P. Genevet, M. A. Kats, F. Aieta, J. Tetienne, F. Capasso, and Z. Gaburro, Light propagation with phase discontinuities: Generalized laws of reflection and refraction, Science **334**, 333 (2011).
[2] B. Assouar, B. Liang, Y. Wu, Y. Li, J. C. Cheng, and Y. Jing, Acoustic metasurfaces, Nat. Rev. Mater. **3**, 460 (2018).
[3] J. Mei and Y. Wu, Controllable transmission and total reflection through an impedance-matched acoustic metasurface, New J. Phys. **16**, 123007 (2014).
[4] Y. Cheng, C. Zhou, B. G. Yuan, D. J. Wu, Q. Wei, and X. J. Liu, Ultra-sparse metasurface for high reflection of low-frequency sound based on artificial Mie resonances, Nat. Mater. **14**, 1013 (2015).
[5] A. Díaz-Rubio and S. A. Tretyakov, Acoustic metasurfaces for scattering-free anomalous reflection and refraction, Phys. Rev. B **96**, 125409 (2017).
[6] J. Li, C. Shen, A. Díaz-Rubio, S. A. Tretyakov, and S. A. Cummer, Systematic design and experimental demonstration of bianisotropic metasurfaces for scattering-free manipulation of acoustic wavefronts, Nat. Commun. **9**, 1342 (2018).
[7] X. Guo, V. E. Gusev, K. Bertoldi, and V. Tournat, Manipulating acoustic wave reflection by a nonlinear elastic metasurface, J. Appl. Phys. **123**, 124901 (2018).
[8] C. Shen, A. Díaz-Rubio, J. Li, and S. A. Cummer, A surface impedance-based three-channel acoustic metasurface retroreflector, Appl. Phys. Lett. **112**, 183503 (2018).
[9] H. Esfahlani, S. Karkar, and H. Lissek, Acoustic carpet cloak based on ultrathin metasurface, Phys. Rev. B **94**, 014302 (2016).
[10] H. Zhang, Y. Xiao, J. Wen, D. Yu, and X. Wen, Ultrathin smart acoustic metasurface for low-frequency sound insulation, Appl. Phys. Lett. **108**, 141902 (2016).
[11] Y. Li and B. M. Assouar, Acoustic metasurface-based perfect absorber with deep subwavelength thickness, Appl. Phys. Lett. **108**, 063502 (2016).
[12] S. Qi, Y. Li, and B. Assouar, Acoustic Focusing and Energy Confinement Based on Multilateral Metasurfaces, Phys. Rev. Appl. **7**, 054006 (2017).
[13] H. Xie and Z. Hou, Nonlocal Metasurface for Acoustic Focusing, Phys. Rev. Appl. **15**, 034054 (2021).
[14] D. Lee, Y. Jang, J. Park, I. S. Kang, J. Li, and J. Rho, Underwater stealth metasurfaces composed of split-orifice–conduit hybrid resonators, J. Appl. Phys. **129**, 105103 (2021).
[15] X. Guo, V. E. Gusev, V. Tournat, B. Deng, and K. Bertoldi, Frequency-doubling effect in acoustic reflection by a nonlinear, architected rotating-square metasurface, Phys. Rev. E **99**, 052209 (2019).
[16] A. V. Kildishev, A. Boltasseva, and V. M. Shalaev, Planar photonics with metasurfaces, Science **339**, 1232009 (2013).
[17] Y. Ra Di, D. L. Sounas, and A. Alù, Metagratings: Beyond the Limits of Graded Metasurfaces for Wave Front Control, Phys. Rev. Lett. **119**, 067404 (2017).
[18] A. Epstein and O. Rabinovich, Unveiling the Properties of Metagratings via a Detailed Analytical Model for Synthesis and Analysis, Phys. Rev. Appl. **8**, 054037 (2017).
[19] D. Torrent, Acoustic anomalous reflectors based on diffraction grating engineering, Phys. Rev. B **98**, 060101 (2018).

[20] Z. Hou, X. Fang, Y. Li, and B. Assouar, Highly Efficient Acoustic Metagrating with Strongly Coupled Surface Grooves, Phys. Rev. Appl. **12**, 034021 (2019).
[21] Y. Fu, C. Shen, Y. Cao, L. Gao, H. Chen, C. T. Chan, S. A. Cummer, and Y. Xu, Reversal of transmission and reflection based on acoustic metagratings with integer parity design, Nat. Commun. **10**, 2326 (2019).
[22] L. Fan and J. Mei, Metagratings for Waterborne Sound: Various Functionalities Enabled by an Efficient Inverse Design Approach, Phys. Rev. Appl. **14**, 044003 (2020).
[23] Y. K. Chiang, S. Oberst, A. Melnikov, L. Quan, S. Marburg, A. Alù, and D. A. Powell, Reconfigurable Acoustic Metagrating for High-Efficiency Anomalous Reflection, Phys. Rev. Appl. **13**, 064067 (2020).
[24] Y. Wang, Y. Cheng, and X. Liu, Modulation of acoustic waves by a broadband metagrating, Sci. Rep. **9**, 7271 (2019).
[25] H. Ni, X. Fang, Z. Hou, Y. Li, and B. Assouar, High-efficiency anomalous splitter by acoustic meta-grating, Phys. Rev. B **100**, 104104 (2019).
[26] L. Fan and J. Mei, Acoustic Metagrating Circulators: Nonreciprocal, Robust, and Tunable Manipulation with Unitary Efficiency, Phys. Rev. Appl. **15**, 064002 (2021).
[27] L. Fan and J. Mei, Multifunctional Waterborne Acoustic Metagratings: From Extraordinary Transmission to Total and Abnormal Reflection, Phys. Rev. Appl. **16**, 044029 (2021).
[28] J. He, X. Jiang, D. Ta, and W. Wang, Experimental demonstration of underwater ultrasound cloaking based on metagrating, Appl. Phys. Lett. **117**, 091901 (2020).
[29] S. Y. Kim, W. Lee, J. S. Lee, and Y. Y. Kim, Longitudinal wave steering using beam-type elastic metagratings, Mech. Syst. Signal Proc. **156**, 107688 (2021).
[30] H. Zhu and F. Semperlotti, Anomalous Refraction of Acoustic Guided Waves in Solids with Geometrically Tapered Metasurfaces, Phys. Rev. Lett. **117**, 034302 (2016).
[31] Y. Liu, Z. Liang, F. Liu, O. Diba, A. Lamb, and J. Li, Source Illusion Devices for Flexural Lamb Waves Using Elastic Metasurfaces, Phys. Rev. Lett. **119**, 034301 (2017).
[32] Y. Chen, X. Li, H. Nassar, G. Hu, and G. Huang, A programmable metasurface for real time control of broadband elastic rays, Smart. Mater. Struct. **27**, 115011 (2018).
[33] X. Li, Y. Chen, R. Zhu, and G. Huang, An active meta-layer for optimal flexural wave absorption and cloaking, Mech. Syst. Signal Proc. **149**, 107324 (2021).
[34] L. Cao, Y. Xu, B. Assouar, and Z. Yang, Asymmetric flexural wave transmission based on dual-layer elastic gradient metasurfaces, Appl. Phys. Lett. **113**, 183506 (2018).
[35] L. Cao, Z. Yang, Y. Xu, S. W. Fan, Y. Zhu, Z. Chen, B. Vincent, and B. Assouar, Disordered Elastic Metasurfaces, Phys. Rev. Appl. **13**, 014054 (2020).
[36] M. S. Kim, W. Lee, C. I. Park, and J. H. Oh, Elastic Wave Energy Entrapment for Reflectionless Metasurface, Phys. Rev. Appl. **13**, 054036 (2020).
[37] G. J. Chaplain, J. M. De Ponti, G. Aguzzi, A. Colombi, and R. V. Craster, Topological Rainbow Trapping for Elastic Energy Harvesting in Graded Su-Schrieffer-Heeger Systems, Phys. Rev. Appl. **14**, 054035 (2020).
[38] S. M. Yuan, A. L. Chen, L. Cao, H. W. Zhang, S. W. Fan, B. Assouar, and Y. S. Wang, Tunable multifunctional fishbone elastic metasurface for the wavefront manipulation of the transmitted in-plane waves, J. Appl. Phys. **128**, 224502 (2020).
[39] Y. Ruan, X. Liang, and C. Hu, Retroreflection of flexural wave by using elastic metasurface, J. Appl. Phys. **128**, 045116 (2020).
[40] B. Li, Y. Hu, J. Chen, G. Su, Y. Liu, M. Zhao, and Z. Li, Efficient Asymmetric Transmission of Elastic waves in Thin Plates with Lossless Metasurfaces, Phys. Rev. Appl. **14**, 054029 (2020).
[41] M. Zheng, C. I. Park, X. Liu, R. Zhu, G. Hu, and Y. Y. Kim, Non-resonant metasurface for broadband elastic wave mode splitting, Appl. Phys. Lett. **116**, 171903 (2020).
[42] J. Rong, W. Ye, S. Zhang, and Y. Liu, Frequency-coded passive multifunctional elastic metasurfaces, Adv. Funct. Mater. **30**, 2005285 (2020).
[43] Y. Jin, W. Wang, A. Khelif, and B. Djafari-Rouhani, Elastic Metasurfaces for Deep and Robust Subwavelength Focusing and Imaging, Phys. Rev. Appl. **15**, 024005 (2021).
[44] Z. Lin and S. Tol, Elastic metasurfaces for full wavefront control and low-frequency energy harvesting, J. Vib. Acoust. **143**, 061005 (2021).
[45] B. Ahn, H. Lee, J. S. Lee, and Y. Y. Kim, Topology optimization of metasurfaces for anomalous reflection of longitudinal elastic waves, Comput. Methods Appl. Mech. Eng. **357**, 112582 (2019).
[46] J. Rong and W. Ye, Multifunctional elastic metasurface design with topology optimization, Acta. Mater. **185**, 382 (2020).
[47] X. Su, Z. Lu, and A. N. Norris, Elastic metasurfaces for splitting SV-and P-waves in elastic solids, J. Appl. Phys. **123**, 091701 (2018).
[48] J. Zhang, X. Su, Y. Pennec, Y. Jing, X. Liu, and N. Hu, Wavefront steering of elastic shear vertical waves in solids via a composite-plate-based metasurface, J. Appl. Phys. **124**, 164505 (2018).
[49] C. Spägele, M. Tamagnone, D. Kazakov, M. Ossiander, M. Piccardo, and F. Capasso, Multifunctional wide-angle optics and lasing based on supercell metasurfaces, Nat. Commun. **12**, 3787 (2021).